Journal of Materials Chemistry A

ROYAL SOCIETY OF CHEMISTRY

PAPER

View Article Online
View Journal | View Issue

Cite this: J. Mater. Chem. A, 2025, 13, 39109

Semiconducting divalent organic spacer-assisted charge transport in lead-free layered perovskites

Waygen Thor, [a] Louise De Cian, [a] Nicolas J. Diercks,[a] Dennis Friedrich, [b] Jun-Ho Yum *[a] and Kevin Sivula *[a]

Received 6th May 2025
Accepted 4th October 2025

DOI: 10.1039/d5ta03603h

rsc.li/materials-a

While employing bulky organic semiconductor cations in layered (2D) hybrid halide perovskites can mitigate dielectric and quantum confinement limitations by enabling charge transfer between organic and inorganic layers, applying this strategy to tin-based perovskites is more challenging due to their more compact structure. Herein, we successfully integrate the strongly π-delocalized naphthalene diimide (NDI) cations with diammonium-functionalized alkyl chain lengths of six carbons (NDI-dH) with tin(II) iodide, forming a layered hybrid organic–inorganic perovskite with a type-II nanoheterojunction electronic architecture. Compared to typical Sn-based hybrid layered perovskite films (prepared with phenylethylamine), the herein reported **(NDI-dH)SnI_4** hybrid perovskite demonstrates significantly improved photogenerated charge carrier lifetime and a notable out-of-plane electron mobility reaching 0.1 $cm^2\ s^{-1}\ V^{-1}$. Additionally, **(NDI-dH)SnI_4** exhibits improved stability in ambient air and nitrogen environments, highlighting its potential for use in air-stable optoelectronic devices.

Introduction

To improve stability and tune the optoelectronic properties of halide perovskites, bulky organic ligands are now often being introduced into the traditional 3D halide perovskites to form hybrid materials with alternating layers of 2D inorganic slabs and organic cations.[1–3] While layered perovskites can generally be classified into two types—Ruddlesden–Popper (RP) and Dion–Jacobson (DJ) phases, they are typically distinguished by their crystal packing[1] and, more recently, the nature of the organic spacer cation.[1,4] RP structures commonly exhibit a shift in the perovskite octahedral slabs and are formed using monovalent organic spacer cations. In contrast, DJ perovskites are formed when divalent spacer cations are employed, enabling a single spacer molecule that bridges adjacent inorganic layers without staggering,[5–7] although shifts in the inorganic slab can still occur.[8]

Employing bulky π-delocalized cations in Pb-based layered hybrid perovskites has been established as a strategy to improve the conductivity and stability, affording materials with potential applications not only in solar energy conversion,[9,10] but also in transistors,[11] light-emitting diodes[12] and other optoelectronic devices.[13,14] Thiophene-[15–18] and pyrene-based[19–21] ammonium cations were among the first π-conjugated organic semiconductor moieties reported to tune the electronic properties in Pb-based systems. More recently, naphthalene diimide-based (NDI) organic semiconductors have received attention from the perovskite community due to their molecular tunability and strong π-electron delocalization, which impart electron-accepting character beneficial for charge transport. However, the strong π–π interactions of NDI offer a challenge for forming the RP or DJ phases. Indeed, NDI functionalized with diethylamide at the nitrogen site of the imide was found to form a 1D metal halide polymorph with a combination of corner-, edge-, and face-sharing modes within the Pb_2I_6 chains.[22–24] In recent work, we successfully showed that employing monovalent NDI-based chromophore cations allows for their incorporation with lead iodide, resulting in the formation of a RP phase layered perovskite.[25,26] Additionally, we have also recently documented the successful synthesis of a DJ layered lead perovskite using divalent dihexylamide-functionalized NDI (NDI-dH), where the hexyl linker length was identified as optimal for the incorporation of the layered perovskite. This structure exhibits improved charge carrier separation properties due to the formation of a type-II electronic nanoheterostructure, which affords the separation of conducting electrons and holes in the organic and inorganic layers, respectively.[27]

Despite these promising reports using Pb-based perovskites, the challenge with the toxicity of lead-based systems needs to be addressed for a more practical implementation of these materials in optoelectronic devices. Tin (Sn^{2+}) offers a less toxic alternative to Pb^{2+}, due to its similar ionic radius and electronic properties.[28,29] Moreover, studies have demonstrated that the

[a]Laboratory for Molecular Engineering of Optoelectronic Nanomaterials (LIMNO), Institut des Sciences et Ingénierie Chimiques (ISIC), École Polytechnique Fédérale de Lausanne (EPFL), 1015 Lausanne, Switzerland. E-mail: junho.yum@epfl.ch; kevin.sivula@epfl.ch

[b]Institute for Solar Fuels, Helmholtz Zentrum Berlin für Materialien und Energie GmbH, Hahn-Meitner-Platz 1, 14109 Berlin, Germany

inclusion of bulky organic ligands helps prevent tin oxidation from Sn^{2+} to Sn^{4+},[30,31] which represents a significant limitation when replacing Pb^{2+} with Sn^{2+}, contributing to improved stability and thus rendering them more viable for practical use. However, efforts toward the incorporation of semiconducting organic ligands into layered Sn^{2+}-based perovskites are far less developed compared to their Pb^{2+} counterparts. Integrating tin with a quaterthiophene-based organic spacer into a type-I nanoheterojunction layered perovskite has been previously reported;[31,32] however, to the best of our knowledge, there is currently no evidence of a type-II nanoheterojunction formed with a layered tin-based perovskite. This emphasizes the potential advantages of incorporating cations with strong π-electron delocalization into tin perovskites, enhancing conductivity while minimizing toxicity.

Herein, we report the formation of a layered tin perovskite with the divalent NDI-dH cation that forms a type-II nanoheterojunction architecture. We observe an enhancement of the out-of-plane electron mobility in **(NDI-dH)SnI_4**, which is one order of magnitude higher than that of layered materials prepared with phenylethylamine, **$(PEA)_2SnI_4$**, along with improved ambient material stability. This significant improvement in the overall performance of tin-based layered perovskites opens opportunities for this class of materials in various applications.

Results and discussion

Thin film formation

In this work, we adopt the classification of layered perovskites based on the nature of the ligand, which has become a practical and widely accepted terminology in the field. As with previous work on Pb-based DJ-type layered perovskites incorporating NDI, optimizing the solution processing conditions including the annealing temperature is critical for incorporating the NDI-dH spacer cation (see the molecular structure in Fig. 1a) into a **(NDI-dH)SnI_4** layered perovskite (shown schematically in Fig. 1b). Starting with typical processing conditions used to prepare thin films of **$(PEA)_2SnI_4$**, *i.e.* spin coating an anhydrous mixture solution of precursors in DMF : DMSO (4 : 1), followed by thermal annealing at 80 °C (see the Experimental section in the SI for full details), X-ray diffraction (XRD) patterns show relatively low intensity reflections of the layered perovskite phase, and the UV-vis absorption spectrum of the thin film also demonstrates only weak shoulder transitions over a scattering baseline (Fig. S1). These data suggest a low crystallinity of the film, with high inhomogeneity. Although a single-step annealing process without an anti-solvent is sufficient for incorporating NDI-dH into the Pb analog,[27] due to the lower formation energy of Sn in comparison to Pb, the use of an anti-solvent treatment and an additional low-temperature annealing step[33] can enhance the crystallinity of the layered perovskite.

Hence, to facilitate optimal incorporation of NDI-dH into a layered tin perovskite, we employed a 2-step spin-coating process followed by a 2-step thermal treatment to fabricate thin films of **(NDI-dH)SnI_4**. After spin coating the DMF : DMSO (4 : 1) precursor solution, chlorobenzene was added as an anti-solvent in a second step. The film was first dried at 50 °C for 10 minutes, followed by a second annealing at 180 °C for the same duration. The two-step thermal treatment is essential for improving the crystallinity of the tin perovskite film, as shown

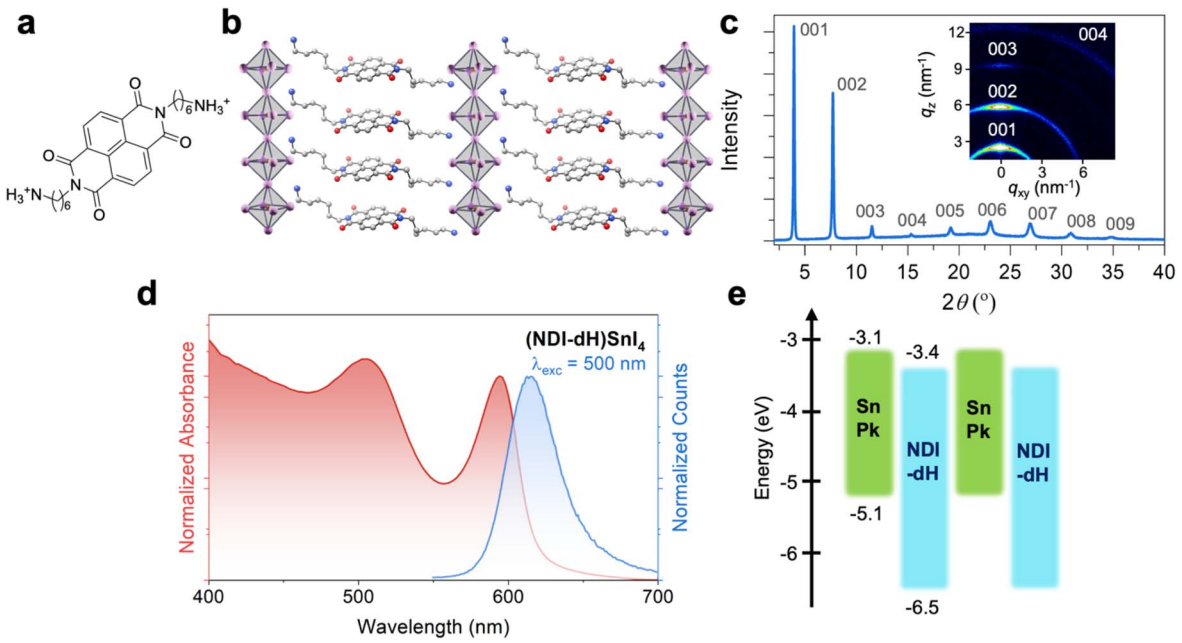

Fig. 1 (a) The chemical structure of divalent dihexylamide-functionalized naphthalene diimide (NDI-dH) used for incorporation. (b) Hypothetical illustration of layered **(NDI-dH)SnI_4** perovskite showing the alternating layers of SnI_4 inorganic slabs and NDI-dH cations. (c) The XRD and uncorrected GIWAXS (inset) patterns of **(NDI-dH)SnI_4**, measured with a Cu Kα1 X-ray source. (d) The absorption (red) and emission spectra (blue) of the **(NDI-dH)SnI_4** film (λ_{exc} = 500 nm). (e) The flat energy level alignments of NDI-dH and the excitonic SnI_4 inorganic slab, as determined from UPS measurements and absorption band edge analysis.

by comparing the XRD patterns of films only annealed at 180 °C (Fig. S1). Likely, the two-step process is advantageous by initiating the crystallization process of slow growth at first, and then allowing rapid growth.[33] The XRD pattern of the optimized **(NDI-dH)SnI_4** thin film (Fig. 1c) exhibits similar reflections to its previously synthesized (NDI-dH)PbI_4 counterpart.[27] A shift of the 001 reflection to smaller 2θ can be observed in the case of **(NDI-dH)SnI_4** compared to the equivalent reflection (002) of **$(PEA)_2SnI_4$** due to the larger cation size (Fig. S2). Besides, the mismatch in the XRD pattern of **(NDI-dH)SnI_4** compared to that of precursor (NDI-dH)I_2 or the 1D analogue NDI-based perovskite suggests the formation of a layered perovskite (Fig. S3). The grazing incidence wide-angle X-ray scattering (GIWAXS) pattern (Fig. 1c, inset) of **(NDI-dH)SnI_4** demonstrates similar reflections to those of the 1D XRD, with stronger intensity along the q_z direction, suggesting a preferentially parallel alignment of the perovskite layers with respect to the substrate. Although a single-crystal structure could not be obtained despite several attempts, the XRD and spectroscopic data are in strong agreement with the assignment of **(NDI-dH)SnI_4** as a layered perovskite.

Basic optoelectronic properties

Turning to the steady state photophysical properties, the UV-vis absorption and photoluminescence emission spectra of **(NDI-dH)SnI_4** (Fig. 1d) exhibit a lowest-energy absorption peak at *ca.* 580 nm and an emission peak at *ca.* 625 nm (500 nm excitation), attributed to exciton recombination. The wide absorption band from 400 nm to 550 nm is assigned to charge transfer transitions between the organic NDI-dH and the inorganic $[SnI_6]^{4-}$.[34] Broadly, these spectra are similar to that of **$(PEA)_2SnI_4$** (Fig. S4). The morphology of the **(NDI-dH)SnI_4** thin film observed with scanning electron microscopy (SEM) shows a typical topology that is commonly observed in layered perovskite materials[35–37] with homogeneous coverage and grains on the order of 100 nm (Fig. S5). Ultraviolet photoelectron spectroscopy (UPS) of **(NDI-dH)SnI_4** reveals a valence band energy of −5.2 eV (Fig. S6). With an excitonic absorption band edge of 2.02 eV (Fig. S7), a type-II nanoheterojunction is likely formed between the Sn-perovskite layers and NDI-dH, as shown schematically in Fig. 1e.[38] In addition, the photoluminescence monitored at the excitonic recombination of **(NDI-dH)SnI_4** is significantly quenched compared to that of **$(PEA)_2SnI_4$** (Fig. S8), further supporting the formation of a type-II nanoheterojunction. This suggests that charge separation can occur upon excitation, with electrons being transferred to and transported within NDI-dH, while holes remain localized in the inorganic slab.

Charge carrier properties

While we acknowledge that multiple factors can influence the band alignment between the energy levels of the organic spacer and the inorganic slabs, and thus the possibility of a type-I architecture cannot be entirely ruled out, we next turn to flash photolysis time-resolved microwave conductivity (fp-TRMC) measurements to elucidate the charge carrier dynamics. The peak sum mobility ($\varphi\sum\mu$) of **(NDI-dH)SnI_4** was measured to be 7.6×10^{-4} cm^2 s^{-1} V^{-1} (at 2.3×10^{12} cm^{-2} absorbed photon flux), comparable to its Pb-analog,[27] and also higher than that of the NDIC2-based 1D Pb perovskite material.[24] However, the $\varphi\sum\mu$ value is lower than that of **$(PEA)_2SnI_4$**, which was measured to be in the range of 10^{-1} cm^2 s^{-1} V^{-1} under similar testing conditions (Fig. S9) consistent with the Pb analog $(PEA)_2PbI_4$.[39] This reduction in $\varphi\sum\mu$ can be attributed to the transfer of electrons to the NDI layer, where they likely have a lower mobility than in the inorganic slabs,[27] although the impact of crystallinity variations cannot be discounted. However, when examining the photogenerated charge carrier lifetime by fp-TRMC, prolonged charge carrier separation is clearly an important factor. Indeed, comparing the photoconductivity transients for both **(NDI-dH)SnI_4** and **$(PEA)_2SnI_4$** (Fig. 2), and fitting each to a bi-exponential decay, significant differences can be observed. The initial time constant of the bi-exponential decay, which is typically attributed to the fast recombination of geminate charge carriers, has a similar value around 30 ns in both materials. In contrast, the second lifetime component is longer in **(NDI-dH)SnI_4** ($\tau = 974 \pm 2$ ns) relative to that of **$(PEA)_2SnI_4$** ($\tau = 489 \pm 1$ ns), which is consistent with a prolonged free charge carrier lifetime due to the effective separation of electrons and holes in **(NDI-dH)SnI_4**, supporting the view that a type-II nanoheterojunction electronic structure is formed in this material.

While the photogenerated charge carrier sum mobility in the direction parallel to the layers was lower in **(NDI-dH)SnI_4** compared to **$(PEA)_2SnI_4$**, the charge carrier mobility lifetime was longer. Hence, we hypothesized that this aspect, together with the relatively close values of energy of the LUMO of NDI-dH and the conduction band of the inorganic slabs, could help in facilitating the movement of charge carriers perpendicular to the layers. To demonstrate this, we fabricated electron-only space charge-limited current (SCLC) thin film devices using a configuration in which the spun-coat perovskite layers were sandwiched between two electron transport layers, *c*-TiO_2 (compact-titanium dioxide) and PCBM ([6,6]-phenyl-C_{61}-butyric acid methyl ester), as depicted in Fig. 3a. A typical current density–voltage (*J–V*) curve of the SCLC device prepared with **(NDI-dH)SnI_4** is displayed in Fig. 3b. A linear dependency of the curve can be found in the low-voltage zone consistent with an ohmic behavior. It is worth noting that no region with $J \propto V^m$, where $m > 3$, was observed. Based on the minimal trap density

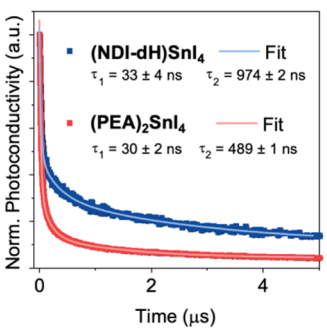

Fig. 2 The fp-TRMC transient decay of (NDI-dH)SnI_4 and $(PEA)_2SnI_4$ at an absorbed photon flux of 10^{12} cm^{-2} ($\lambda_{exc} = 500$ nm).

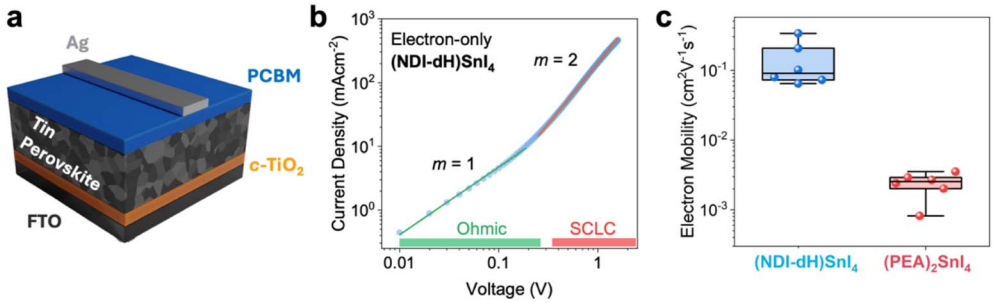

Fig. 3 (a) The device architecture of electron-only SCLC measurement and (b) the resulting SCLC J–V curve obtained for **(NDI-dH)SnI$_4$**. (c) The comparison of the electron mobility obtained for **(NDI-dH)SnI$_4$** and **(PEA)$_2$SnI$_4$**.

equation (see the Characterization section of the SI),[40,41] this phenomenon indicates that the trap density in the **(NDI-dH)SnI$_4$** film is below the minimal value, n_{min} of 3.31×10^{14} cm^{-3}.

Based on the SCLC region of the J–V curve ($m = 2$ region), the electron mobility of **(NDI-dH)SnI$_4$** was found to be in the range of 10^{-1} to 10^{-2} cm^2 s^{-1} V^{-1}, as calculated using the Mott–Gurney law, and is reproducible over many measurements (Fig. 3c). In contrast, the electron mobility of **(PEA)$_2$SnI$_4$** was consistently estimated to be order of magnitude lower in the range of 10^{-3} cm^2 s^{-1} V^{-1}, as shown in Fig. 3c (see Fig. S10 for the J–V curve), which is typical for layered perovskites with small insulating organic spacers.[42] Since the estimated electron mobility derived from SCLC measurements is highly dependent on the thickness of the active semiconducting layer, we verified our mobility estimation by altering the film thickness (*via* the deposition solution concentration, see cross-sectional SEM images in Fig. S11).[43] We achieved electron mobility values in a comparable range for different thicknesses (Fig. S12), further substantiating our results.

Overall, we note that our observation of a higher electron mobility in **(NDI-dH)SnI$_4$** compared to that of **(PEA)$_2$SnI$_4$**, as measured using SCLC, and the opposite trend when comparing the TRMC measurements, is not surprising given the high-intensity reflections along the q_z direction observed in the GIWAXS patterns of **(PEA)$_2$SnI$_4$** films, which suggest a strongly preferred parallel orientation of the layers to the substrate (Fig. S13). Since our TRMC setup measures the carrier mobility locally and parallel to the substrate,[44,45] the highly oriented and larger grain size of the **(PEA)$_2$SnI$_4$** film compared to that of **(NDI-dH)SnI$_4$** (see Table S1 for a quantitative comparison) contributes to higher sum mobility, as fewer grain boundaries hinder charge transport when moving parallel to the substrate.[46] In contrast, from a macroscopic perspective in SCLC, where mobilities are assessed perpendicular to the film (out-of-plane electron mobility),[40] **(NDI-dH)SnI$_4$** exhibits enhanced electron transport across the layers due to the type-II nanoheterojunction and alignment of the conduction energy levels. Besides electron mobility, this can be further evidenced by the higher SCLC hole mobilities (Fig. S14), which, similar to the electron mobilities, are also one order of magnitude higher than those of the control **(PEA)$_2$SnI$_4$**.

Material stability

While the enhanced optoelectronic properties establish the potential of **(NDI-dH)SnI$_4$** towards possible device applications, the stability of the material under ambient conditions is critically important for practical implementation. Therefore, we investigated the influence of NDI-dH incorporation on the stability of the tin perovskite. Upon extended exposure to ambient air conditions, films of **(NDI-dH)SnI$_4$** appeared more stable compared to the control **(PEA)$_2$SnI$_4$**. As demonstrated in Fig. 4a, the absorption spectra of **(NDI-dH)SnI$_4$** change minimally when exposed for over 60 min, while the absorption of **(PEA)$_2$SnI$_4$** drastically decreased over the same time. The difference in stability can also be seen by naked eye observation, which shows the bleaching of **(PEA)$_2$SnI$_4$** after a few hours, while the color of **(NDI-dH)SnI$_4$** remains relatively more stable over two days (Fig. S15). This visual observation is further supported by XRD measurements over time, which confirm that **(NDI-dH)SnI$_4$** retains its layered perovskite structure, whereas **(PEA)$_2$SnI$_4$** shows clear signs of degradation (Fig. S16). Moreover, while degradation of **(PEA)$_2$SnI$_4$** also occurs when stored under a nitrogen atmosphere,[31] the intensity of the absorption of **(NDI-dH)SnI$_4$** remains fairly unchanged even after two weeks being stored in a N_2 glove box (Fig. S17). The content of Sn^{4+} in the fresh **(NDI-dH)SnI$_4$** and **(PEA)$_2$SnI$_4$** films, exposed to air only briefly for sample transfer, was compared using X-ray photoelectron spectroscopy (XPS). The two deconvoluted peaks can be assigned as Sn^{2+} and Sn^{4+}, with Sn^{4+} at a higher energy level

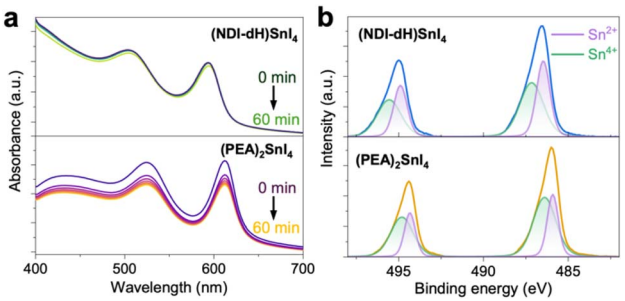

Fig. 4 (a) Time-dependent absorption spectra of **(NDI-dH)SnI$_4$** and **(PEA)$_2$SnI$_4$** recorded over 60 minutes under ambient conditions, with measurements taken at 10-minute intervals. (b) The XPS spectra measured at the Sn energy level, with the deconvolution of the peak into Sn^{2+} and Sn^{4+} for **(PEA)$_2$SnI$_4$** and **(NDI-dH)SnI$_4$**.

(Fig. 4b). While we acknowledge that some oxidation may have occurred during sample transfer, both samples were treated identically. The relative concentration of Sn^{4+} in **(NDI-dH)SnI_4** is much lower compared to that in **$(PEA)_2SnI_4$** (see relative values in Table S2), indicating that the oxidation of Sn^{2+} is less prevalent in the former. The enhanced stability of **(NDI-dH)SnI_4** may be due to a difference in oxygen molecule diffusion, which could likely be more sterically hindered by the bulky NDI-dH surface layer, preventing the decomposition of the perovskite. Furthermore, unlike the monovalent spacer in **$(PEA)_2SnI_4$**, the layered **(NDI-dH)SnI_4** with divalent coordination of the spacer lacks van der Waals gaps between organic spacers. This structural difference likely also contributes to its enhanced stability, consistent with previous reports demonstrating superior stability with divalent coordinated perovskites compared to their monovalent analogues.[47,48]

Conclusion

In conclusion, we have demonstrated the successful incorporation of a divalent spacer including a semiconducting naphthalene diimide with tin iodide to form a lead-free layered tin perovskite **(NDI-dH)SnI_4**. In comparison to the commonly used **$(PEA)_2SnI_4$**, the longer charge carrier mobility lifetime observed through TRMC suggests that layered perovskite forms a type-II energy level architecture that facilitates charge separation. This, together with the close alignment of the conduction energy levels of the inorganic and organic slabs, allows electron transport perpendicular to the layers. The measured out-of-plane electron mobility for **(NDI-dH)SnI_4** is at least one order greater than that of the **$(PEA)_2SnI_4$** based on SCLC measurements. Alongside the electron transport properties, **(NDI-dH)SnI_4** exhibits superior stability compared to **$(PEA)_2SnI_4$** under both inert and ambient air conditions. The improved electronic properties and stability of this layered hybrid organic–inorganic lead-free perovskite highlight its promise for use in air-stable Sn-based optoelectronic devices.

Author contributions

W. T. wrote the draft after scientific discussion with J. H. Y. and K. S. K. S. and J. H. Y. supervised the project. Synthesis of the cations, thin films fabrications and characterization studies were performed by W. T. with help from L. D. C. and N. J. D. The fp-TRMC measurements were performed by L. D. C. and D. F. All authors have given approval to the final version of the manuscript.

Conflicts of interest

There are no conflicts to declare.

Data availability

Data for this article, including data tables used to create figures in the main text, are available on Zenodo at **https://doi.org/10.5281/zenodo.15348904**.

Supplementary information: experimental information, Fig. S1–S16, and Tables S1 and S2 as described in the main text. See DOI: **https://doi.org/10.1039/d5ta03603h**.

Acknowledgements

The authors graciously acknowledge the technical support of Dr Mounir Mensi for the UPS and XPS measurements. Support from the School of Basic Sciences at EPFL is also acknowledged.

References

1 X. Li, J. M. Hoffman and M. G. Kanatzidis, *Chem. Rev.*, 2021, **121**, 2230–2291.
2 L. Pedesseau, D. Sapori, B. Traore, R. Robles, H.-H. Fang, M. A. Loi, H. Tsai, W. Nie, J.-C. Blancon, A. Neukirch, S. Tretiak, A. D. Mohite, C. Katan, J. Even and M. Kepenekian, *ACS Nano*, 2016, **10**, 9776–9786.
3 C. Ortiz-Cervantes, P. Carmona-Monroy and D. Solis-Ibarra, *ChemSusChem*, 2019, **12**, 1560–1575.
4 D. Ghosh, D. Acharya, L. Pedesseau, C. Katan, J. Even, S. Tretiak and A. J. Neukirch, *J. Mater. Chem. A*, 2020, **8**, 22009–22022.
5 A. Dučinskas, M. Jung, Y.-R. Wang, J. V. Milić, D. Moia, M. Grätzel and J. Maier, *J. Mater. Chem. C*, 2024, **12**, 7909–7915.
6 S. Min and J. Cho, *Adv. Opt. Mater.*, 2024, **12**, 2302516.
7 C. Chen, J. Xu, X. Wang and R. G. Palgrave, *J. Mater. Chem. A*, 2024, **12**, 5055–5079.
8 X. Li, W. Ke, B. Traoré, P. Guo, I. Hadar, M. Kepenekian, J. Even, C. Katan, C. C. Stoumpos, R. D. Schaller and M. G. Kanatzidis, *J. Am. Chem. Soc.*, 2019, **141**, 12880–12890.
9 H. Tsai, W. Nie, J.-C. Blancon, C. C. Stoumpos, R. Asadpour, B. Harutyunyan, A. J. Neukirch, R. Verduzco, J. J. Crochet, S. Tretiak, L. Pedesseau, J. Even, M. A. Alam, G. Gupta, J. Lou, P. M. Ajayan, M. J. Bedzyk, M. G. Kanatzidis and A. D. Mohite, *Nature*, 2016, **536**, 312–316.
10 C. Liang, H. Gu, Y. Xia, Z. Wang, X. Liu, J. Xia, S. Zuo, Y. Hu, X. Gao, W. Hui, L. Chao, T. Niu, M. Fang, H. Lu, H. Dong, H. Yu, S. Chen, X. Ran, L. Song, B. Li, J. Zhang, Y. Peng, G. Shao, J. Wang, Y. Chen, G. Xing and W. Huang, *Nat. Energy*, 2021, **6**, 38–45.
11 C. Liao, S. Bernardi, C. G. Bailey, I. H. Chao, S.-Y. Chien, G. Wang, Y.-H. Sun, S. Tang, J. Zheng, J. Yi, M.-H. Yu, S. P. Russo, H.-W. Yen, D. R. McCamey, B. J. Kennedy, A. Widmer-Cooper, C.-C. Chueh and A. W. Y. Ho-Baillie, *ACS Nano*, 2024, **18**, 14176–14186.
12 N. Wang, L. Cheng, R. Ge, S. Zhang, Y. Miao, W. Zou, C. Yi, Y. Sun, Y. Cao, R. Yang, Y. Wei, Q. Guo, Y. Ke, M. Yu, Y. Jin, Y. Liu, Q. Ding, D. Di, L. Yang, G. Xing, H. Tian, C. Jin, F. Gao, R. H. Friend, J. Wang and W. Huang, *Nat. Photonics*, 2016, **10**, 699–704.
13 T. Huang, R. Li, X. Chen, Y. Li, Y. Chang, W. Li and W. Yu, *ACS Appl. Electron. Mater.*, 2023, **5**, 2169–2177.
14 C. Qin, A. S. D. Sandanayaka, C. Zhao, T. Matsushima, D. Zhang, T. Fujihara and C. Adachi, *Nature*, 2020, **585**, 53–57.

15 Y. Gao, E. Shi, S. Deng, S. B. Shiring, J. M. Snaider, C. Liang, B. Yuan, R. Song, S. M. Janke, A. Liebman-Peláez, P. Yoo, M. Zeller, B. W. Boudouris, P. Liao, C. Zhu, V. Blum, Y. Yu, B. M. Savoie, L. Huang and L. Dou, *Nat. Chem.*, 2019, **11**, 1151–1157.
16 J. Y. Park, R. Song, J. Liang, L. Jin, K. Wang, S. Li, E. Shi, Y. Gao, M. Zeller, S. J. Teat, P. Guo, L. Huang, Y. S. Zhao, V. Blum and L. Dou, *Nat. Chem.*, 2023, **15**, 1745–1753.
17 D. Lu, G. Lv, Z. Xu, Y. Dong, X. Ji and Y. Liu, *J. Am. Chem. Soc.*, 2020, **142**, 11114–11122.
18 C. Ni, Y. Huang, T. Zeng, D. Chen, H. Chen, M. Wei, A. Johnston, A. H. Proppe, Z. Ning, E. H. Sargent, P. Hu and Z. Yang, *Angew. Chem., Int. Ed.*, 2020, **59**, 13977–13983.
19 A. De, C. Mora Perez, A. Liang, K. Wang, L. Dou, O. Prezhdo and L. Huang, *J. Am. Chem. Soc.*, 2024, **146**, 4260–4269.
20 J. V. Passarelli, D. J. Fairfield, N. A. Sather, M. P. Hendricks, H. Sai, C. L. Stern and S. I. Stupp, *J. Am. Chem. Soc.*, 2018, **140**, 7313–7323.
21 J. Xue, R. Wang, X. Chen, C. Yao, X. Jin, K.-L. Wang, W. Huang, T. Huang, Y. Zhao, Y. Zhai, D. Meng, S. Tan, R. Liu, Z.-K. Wang, C. Zhu, K. Zhu, M. C. Beard, Y. Yan and Y. Yang, *Science*, 2021, **371**, 636–640.
22 A. H. Proppe, M.-H. Tremblay, Y. Zhang, Z. Yang, R. Quintero-Bermudez, S. O. Kelley, S. Barlow, S. R. Marder and E. H. Sargent, *J. Phys. Chem. C*, 2020, **124**, 24379–24390.
23 H. Fang, F.-H. Chen, S.-Q. Zhang and M.-J. Lin, *Inorg. Chem.*, 2023, **62**, 9661–9670.
24 E. Amerling, Y. Zhai, B. W. Larson, Y. Yao, B. Fluegel, Z. Owczarczyk, H. Lu, L. Whittaker-Brooks, V. Blum and J. L. Blackburn, *J. Mater. Chem. A*, 2021, **9**, 14977–14990.
25 S. Nussbaum, D. Tsokkou, A. T. Frei, D. Friedrich, J.-E. Moser, N. Banerji, J.-H. Yum and K. Sivula, *J. Am. Chem. Soc.*, 2024, **146**, 27770–27778.
26 S. Nussbaum, E. Socie, L. Yao, J.-H. Yum, J.-E. Moser and K. Sivula, *Chem. Mater.*, 2022, **34**, 3798–3805.
27 S. Nussbaum, E. Socie, G. C. Fish, N. J. Diercks, H. Hempel, D. Friedrich, J.-E. Moser, J.-H. Yum and K. Sivula, *Chem. Sci.*, 2023, **14**, 6052–6058.
28 J. Cao and F. Yan, *Energy Environ. Sci.*, 2021, **14**, 1286–1325.
29 W. Ke, C. C. Stoumpos and M. G. Kanatzidis, *Adv. Mater.*, 2019, **31**, 1803230.
30 W. Park, Y. Reo, W. Yang, H. Choi, S. Jeon, B. Lim, A. Liu, H. Zhu and Y.-Y. Noh, *ACS Energy Lett.*, 2024, **9**, 2436–2445.
31 Y. Gao, Z. Wei, P. Yoo, E. Shi, M. Zeller, C. Zhu, P. Liao and L. Dou, *J. Am. Chem. Soc.*, 2019, **141**, 15577–15585.
32 K. Wang, L. Jin, Y. Gao, A. Liang, B. P. Finkenauer, W. Zhao, Z. Wei, C. Zhu, T.-F. Guo, L. Huang and L. Dou, *ACS Nano*, 2021, **15**, 6316–6325.
33 H. Yao, T. Wu, Y. Xiao, L. Ding, Y. Hua and F. Hao, *ACS Mater. Lett.*, 2023, **5**, 3203–3211.
34 H. Ji, X. Liu, L. Li, F. Zhang, L. Qin, Z. Lou, D. Li, Y. Hu, Y. Hou and F. Teng, *J. Mater. Chem. A*, 2023, **11**, 7767–7779.
35 V. E. Madhavan, I. Zimmermann, A. A. B. Baloch, A. Manekkathodi, A. Belaidi, N. Tabet and M. K. Nazeeruddin, *ACS Appl. Energy Mater.*, 2020, **3**, 114–121.
36 L. Kuai, J. Li, Y. Li, Y. Wang, P. Li, Y. Qin, T. Song, Y. Yang, Z. Chen, X. Gao and B. Sun, *ACS Energy Lett.*, 2020, **5**, 8–16.
37 L. Gao, F. Zhang, C. Xiao, X. Chen, B. W. Larson, J. J. Berry and K. Zhu, *Adv. Funct. Mater.*, 2019, **29**, 1901652.
38 A. Dey, A. Kalita and P. Krishnan Iyer, *ACS Appl. Mater. Interfaces*, 2014, **6**, 12295–12301.
39 F. Zhang, D. H. Kim, H. Lu, J.-S. Park, B. W. Larson, J. Hu, L. Gao, C. Xiao, O. G. Reid, X. Chen, Q. Zhao, P. F. Ndione, J. J. Berry, W. You, A. Walsh, M. C. Beard and K. Zhu, *J. Am. Chem. Soc.*, 2019, **141**, 5972–5979.
40 V. M. Le Corre, E. A. Duijnstee, O. El Tambouli, J. M. Ball, H. J. Snaith, J. Lim and L. J. A. Koster, *ACS Energy Lett.*, 2021, **6**, 1087–1094.
41 J. A. Röhr, T. Kirchartz and J. Nelson, *J. Phys. Condens. Matter*, 2017, **29**, 205901.
42 Y. Li, J. V. Milić, A. Ummadisingu, J.-Y. Seo, J.-H. Im, H.-S. Kim, Y. Liu, M. I. Dar, S. M. Zakeeruddin, P. Wang, A. Hagfeldt and M. Grätzel, *Nano Lett.*, 2019, **19**, 150–157.
43 K. Sivula, *ACS Energy Lett.*, 2022, **7**, 2102–2104.
44 N. K. Tailor, Yukta, R. Ranjan, S. Ranjan, T. Sharma, A. Singh, A. Garg, K. S. Nalwa, R. K. Gupta and S. Satapathi, *J. Mater. Chem. A*, 2021, **9**, 21551–21575.
45 J. Peng, Y. Chen, K. Zheng, T. Pullerits and Z. Liang, *Chem. Soc. Rev.*, 2017, **46**, 5714–5729.
46 A. Liang, Y. Gao, R. Asadpour, Z. Wei, B. P. Finkenauer, L. Jin, J. Yang, K. Wang, K. Chen, P. Liao, C. Zhu, L. Huang, B. W. Boudouris, M. A. Alam and L. Dou, *J. Am. Chem. Soc.*, 2021, **143**, 15215–15223.
47 P. Huang, S. Kazim, M. Wang and S. Ahmad, *ACS Energy Lett.*, 2019, **4**, 2960–2974.
48 S. Ahmad, P. Fu, S. Yu, Q. Yang, X. Liu, X. Wang, X. Wang, X. Guo and C. Li, *Joule*, 2019, **3**, 794–806.